Penerbit Akademia Baru

CFD Letters

Journal homepage: www.akademiabaru.com/cfdl.html
ISSN: 2180-1363

Numerical Examination on Two-Equations Turbulence Models for Flow Across NACA 0012 Airfoil with Different Angle of Attack

Open Access

Yu Han Ng[1], Wah Yen Tey[1,2,*], Lit Ken Tan[2], Gerald Pacaba Arada[3], M.W. Muhieldeen[1]

[1] Department of Mechanical Engineering, Faculty of Engineering, UCSI University, Kuala Lumpur, Malaysia
[2] Takasago i-Kohza, Malaysia-Japan International Institute of Technology, Universiti Teknologi Malaysia, Kuala Lumpur, Malaysia
[3] Gokongwei College of Engineering, De La Salle University, Manila, Philippines

ARTICLE INFO

Article history:
Received 21 December 2019
Received in revised form 17 February 2020
Accepted 22 February 2020
Available online 28 February 2020

ABSTRACT

Selection of an appropriate and efficient turbulence models is important for fast and accurate computation in fluid dynamics. In order to investigate the computational efficiency of turbulence models, numerical examination based on two-equations turbulence models for flow across NACA 0012 airfoil was carried out by using ANSYS Fluent at various angle of attack (-12° to 20°) and at a Reynold number of 3×10^6. The case study is chosen as its transition from viscid to inviscid flow region which would put a strain on computational performance of turbulence models. The two-equation models being investigated are Standard *k-ε* model, RNG *k-ε* model, *k-ε* Realizable model, Standard *k-ω* model, *k-ω* BSL model and *k-ω* SST model. The drag, lift and pressure coefficient between simulation and experimental results are compared. The convergence rate of these turbulence models is collated as well. The contours of static pressure and velocity magnitude was simulated, and boundary layer separation was noticed from 10° angle of attack. In general, the predicted data have good agreement with experimental data. Amongst the investigated models, *k-ω* SST model showed the best agreement with experimental result meanwhile RNG *k-ε* model showed the slowest convergence rate among all the turbulence models.

Keywords:
Two-equations models; Reynolds-Averaged Navier-Stokes Equations (RANS); Ansys Fluent; Flow across Airfoil; NACA 0012

1. Introduction

Turbulent flow is three-dimensional, unpredictable fluid flow phenomenon which is highly diffusive and dissipative, in which the eddies are prevalent across the flow [1]. Indeed, there are many natural phenomenon and scientific case studies which involve flow turbulence, such as the turbulence in ocean and wind turbine [2-3], engineering piping [4-5], flow-induced vibration [6-7] and operation of bioreactor [8-9]. Transition from a smooth laminar flow to a chaotic turbulent flow

* *Corresponding author.*
E-mail address: teywy@ucsiuniversity.edu.my (Wah Yen Tey)

would give rise to complex fluid dynamics phenomenon, which would involve the mixing of fluids, dissipation of energy and increment of drag.

With the advancement of Computational Fluid Dynamics (CFD), various methods have been introduced and widely applied to predict the nature of turbulence. Basically, turbulent flow can be investigated using three main methods: Direct Eddy Simulation (DNS), Large Eddy Simulation (LES) and turbulence modelling based on Reynolds-Averaged Navier-Stokes (RANS) equation [10]. DNS solves the all the spatial and temporal scale of turbulence down to Kolmogorov scale, and therefore it would render a result with superior accuracy. However, it calls upon a very large computational memory and most of the DNS studies are still limited to low Re flow [11–14]. In LES, the analysis on small eddies is replaced with other models such as wall adapting local eddy viscosity model [15], mixed time scale model [16] and parabolised stability equations [17]. Compared with the DNS computation cost of $Re^{2.64}$, it is only $Re^{1.85}$ for LES [18]. This has enabled the simulation on a flow with higher Re and been evinced in the recent works of Kim *et al.,* [17], Badoe *et al.,* [19], Arora *et al.,* [20] and Toubiana *et al.,* [21]. Meanwhile, the turbulence modelling based on RANS would have the lowest computation cost with the sacrifice of results' accuracy. Mathematical details of RANS and its turbulence models will be explained in the next section. The review on these three methods can be referred to the literature by Argyropoulos and Markatos [22].

Two-equations turbulence modelling approach is one of the most popular methods being applied for turbulence prediction as it can greatly simplify the complex flow in practical [1]. Since many turbulent models have been introduced, selection of a robust model is critical for CFD simulation. In this study, six two-equations turbulent models (Standard *k-ε*, RNG *k-ε*, *k-ε* Realisable, Standard *k-ω*, *k-ω* BSL and *k-ω* SST) are considered to simulate the flow across NACA 0012 airfoil. The co-existence of viscid and inviscid flow regions makes the case study an excellent platform to assess their computational performance. Finite volume based commercial software ANSYS Fluent was applied in current study. Pressure coefficient, drag coefficient and lift coefficient are analysed at different angle of attack at Re = 3×10^6 and compared with experiment data. The pressure-velocity contours are computed while convergence performance of these models is compared too.

2. Methodology

2.1 Reynold-Averaged Navier-Stokes equations (RANS)

Consider the conventional Continuity and momentum equations which govern the flow of viscous incompressible fluid as:

$$\frac{\partial u_i}{\partial x_i} = 0 \tag{1}$$

$$\rho\left(\frac{\partial u_i}{\partial t} + \frac{\partial\left(u_i u_j\right)}{\partial x_j}\right) = -\frac{\partial P}{\partial x_i} + \frac{\partial\left(2\mu S_{ij}\right)}{\partial x_i} \tag{2}$$

where u_i and u_j is flow velocity while ρ is fluid density. The strain-rate tensor, S_{ij} for Newtonian fluid can be defined as in Eq. (3). By inserting Eq. (3) into (1), Eq. (4) can be formed.

$$S_{ij} = \frac{1}{2}\left(\frac{\partial u_i}{\partial x_j} + \frac{\partial u_j}{\partial x_i}\right) \tag{3}$$

$$\rho\left(\frac{\partial u_i}{\partial t}+\frac{\partial\left(u_i u_j\right)}{\partial x_j}\right)=-\frac{\partial P}{\partial x_i}+\frac{\partial^2 u_i}{\partial x_j} \tag{4}$$

In turbulent flow, the fields become random functions of space and time. Thus, the variables of u_i and P can be divided into mean part and fluctuating part as:

$$u_i=\overline{u_i}+u_i' \ , \ P_i=\overline{P_i}+P_i' \tag{5}$$

Since it is not necessary to concern all the detail of turbulence fluctuations, the RANS equations can be formed by averaging the equations:

$$u_i'=0\rightarrow u_i=\overline{u_i} \tag{6}$$

$$P_i'=0\rightarrow P_i=\overline{P_i} \tag{7}$$

By substituting Eq. (5) into Eqs. (1) and (2), Continuity and momentum equations become:

$$\frac{\partial\overline{u_i}}{\partial x_i}=0 \tag{8}$$

$$\rho\left(\frac{\partial\overline{u_i}}{\partial t}+\frac{\partial\left(\overline{u_i u_j}\right)}{\partial x_j}\right)=-\frac{\partial P}{\partial x_i}+\frac{\partial}{\partial x_j}\left(2\mu\overline{S_{ij}}-\rho\overline{u_i' u_j'}\right) \tag{9}$$

and mean strain-rate tensor S_{ij} becomes:

$$S_{ij}=\frac{1}{2}\left(\frac{\partial\overline{u_i}}{\partial x_j}+\frac{\partial\overline{u_j}}{\partial x_i}\right) \tag{10}$$

By combining Eqs. (8) to (10), the momentum equations can be expressed as:

$$\frac{\partial\overline{u_i}}{\partial t}+\overline{u_j}\frac{\partial\left(\overline{u_i u_j}\right)}{\partial x_j}=-\frac{\partial P}{\partial x_i}+\nu\left(\frac{\partial^2\overline{u_i}}{\partial x_i\partial x_j}-\frac{\partial\tau_{ij}}{\partial x_j}\right) \tag{11}$$

where τ_{ij} is the Reynold's stress tensor. By devising the instantaneous properties into mean and fluctuating parts, 3 unknown quantities were appeared. Unfortunately, that are no any additional equation to gain. Hence, this system is not a closed system. In order to solve the closure problem, the various types of turbulence models were applied to close the RANS equation by predicting the turbulent viscosity. RANS equations require closure for Reynolds stress and the effect of turbulence can be presented as an eddy viscosity.

$$\tau_{ij} = -\overline{u_i u_j} = 2\mu_t S_{ij} - \frac{2}{3}k\delta_{ij} \tag{12}$$

where μ_t is the kinetic eddy viscosity, δ_{ij} is Kronecker delta and k is the turbulence kinetic energy which can be defined as:

$$k = \frac{1}{2}\overline{u_i u_j} \tag{13}$$

In order to close the equations, turbulence models are required. In the following section, the formulation of Standard k-ε, RNG k-ε, k-ε Realisable, standard k-ω, k-ω BSL and k-ω SST will be explained.

2.2 Turbulence Models

2.2.1 Standard k-ε model

The original Standard *k-ε* model was proposed by Launder and Spalding [23]. In Standard k-ε model, turbulent kinetic energy k and dissipation rate ε can be defined as in Eqs. (14) and (15) respectively.

$$\frac{\partial(\rho k)}{\partial t} + \frac{\partial(\rho k u_i)}{\partial x_i} = \frac{\partial}{\partial x_i}\left[\left(\mu + \frac{\mu_t}{\sigma_k}\right)\frac{\partial k}{\partial x_j}\right] + G_k + G_b - \rho\varepsilon - Y_M + S_k \tag{14}$$

$$\frac{\partial(\rho \varepsilon)}{\partial t} + \frac{\partial(\rho \varepsilon u_i)}{\partial x_i} = \frac{\partial}{\partial x_i}\left[\left(\mu + \frac{\mu_t}{\sigma_\varepsilon}\right)\frac{\partial \varepsilon}{\partial x_j}\right] + C_{1\varepsilon}\frac{\varepsilon}{k}\left(G_k + C_{3\varepsilon}G_b\right) - C_{2\varepsilon}\rho\frac{\varepsilon^2}{k} + S_\varepsilon \tag{15}$$

The turbulent viscosity μ_t can calculated from formula as:

$$\mu_t = \rho c_\mu \frac{k^2}{\varepsilon} \tag{16}$$

while G_k is the generation of turbulent kinetic energy due to the mean velocity gradient, which can be defined as:

$$G_k = -\rho\overline{u_i u_j}\frac{\partial u_j}{\partial x_i} \tag{17}$$

G_b is the generation of turbulent kinetic energy due to buoyancy and Y_M is the contribution of the fluctuating dilation in compressible turbulence to overall dissipation rate, and they can be defined in Eqs. (18) and (19) respectively.

$$G_k = \beta g_i \frac{\partial \mu_t}{\partial x_i} \tag{18}$$

$$Y_M = 2\rho\varepsilon M_t^{\,2} \tag{19}$$

S_k and S_ε are user sources term. σ_ε is the turbulent Prandtl number of the dissipation rate and σ_k is the turbulent Prandtl number of the turbulent kinetic energy. The standard values of the constant which obtained experimentally are: $C_\mu = 0.09$, $C_{1\varepsilon} = 1.44$, $C_{2\varepsilon} = 1.92$ while $\sigma_\varepsilon = 1.3$.

2.2.2 RNG k-ε model

RNG *k-ε* model is quite similar to standard k-ε model. The only different is that RNG *k-ε* model uses a technique renormalization group theory [24] but Standard *k-ε* model does not. The new terms were added into to the transport equation for dissipation rate and turbulent kinetic energy. This helped the RNG model to improve the accuracy of swirling flow. The transport equation for turbulent kinetic energy *k* and dissipation rate *ε* is:

$$\frac{\partial(\rho k)}{\partial t} + \frac{\partial(\rho k u_i)}{\partial x_i} = \frac{\partial}{\partial x_i}\left(\alpha_k \mu_{eff} \frac{\partial k}{\partial x_j}\right) + G_k + G_b - \rho\varepsilon - Y_M + S_k \tag{20}$$

$$\frac{\partial(\rho \varepsilon)}{\partial t} + \frac{\partial(\rho \varepsilon u_i)}{\partial x_i} = \frac{\partial}{\partial x_i}\left[\alpha_\varepsilon \mu_{eff} \frac{\partial \varepsilon}{\partial x_j}\right] + C_{1\varepsilon}\frac{\varepsilon}{k}\left(G_k + C_{3\varepsilon}G_b\right) - C_{2\varepsilon}\rho\frac{\varepsilon^2}{k} - R_\varepsilon + S_\varepsilon \tag{21}$$

where α_ε is the inverse effective turbulent Prandtl number of the dissipation rate and α_k is the inverse effective turbulent Prandtl number of the turbulent kinetic energy. In RNG model, the turbulent viscosity v_t was obtained effectively by a scale elimination procedure as:

$$d\left(\frac{\rho^2 k}{\sqrt{\varepsilon\mu}}\right) = 1.72\frac{\hat{v}}{\sqrt{\hat{v}^3 - 1 + C_v}}d\hat{v} \tag{22}$$

This equation is used to determine the accurate description of how the effective turbulent transport varies with effective Reynold number to determine better accuracy result in near-wall flow and low-Re number flow. Thus, RNG model should give a more accurate result. However, the formula of turbulence viscosity in high-Re number is same as standard model as in Eq. (16). Although the formula is same as standard model, C_μ of RNG model has a different value with standard model. The C_μ in RNG model is 0.0845 which is very close to standard model (0.09). The standard values of the constant which obtained experimentally are: $C_\mu = 0.0845$, $C_{1\varepsilon} = 1.42$ while $C_{2\varepsilon} = 1.68$.

2.2.3 k-ε Realisable model

k-ε Realisable model is the newest model in *k-ε* variation. It was developed by Shih *et al.,* [25]. This model is different with Standard *k-ε* model in terms of turbulent viscosity and transport equation for dissipation rate ε was. This new transport equation for dissipation rate was derived from the equation for the transport of the mean-square vorticity fluctuation. Thus, *k-ε* Realisable model is more suitable to use in predicting separate flows and flows with complex secondary flow feature. The turbulent kinetic energy *k* of *k-ε* Realisable model is same with standard k- ε model as in Eq. (14) while its dissipation rate *ε* equation is in Eq. (23).

$$\frac{\partial(\rho\varepsilon)}{\partial t}+\frac{\partial(\rho\varepsilon u_j)}{\partial x_j}=\frac{\partial}{\partial x_i}\left[\mu+\left(\frac{\mu_t}{\sigma_\varepsilon}\right)\frac{\partial\varepsilon}{\partial x_j}\right]+\rho C_1 S\varepsilon-C_2\rho\frac{\varepsilon^2}{k+\sqrt{\upsilon\varepsilon}}+C_{1e}\rho\frac{\varepsilon}{k}C_{3e}G_b+S_e \tag{23}$$

The turbulent viscosity of realizable model is same with the other *k-ε* models as in Eq. (16). However, C_μ is not a constant in realizable model and can calculated from formula:

$$C_\mu=\frac{1}{A_0+A_S\frac{kU^*}{\varepsilon}} \tag{24}$$

$$U^*=\sqrt{S_{ij}S_{ij}+\Omega_{ij}\Omega_{ij}} \tag{25}$$

$$\Omega_{ij}=\overline{\Omega_{ij}}-3\varepsilon_{ijk}\omega_k \tag{26}$$

where $\overline{\Omega_{ij}}$ is the mean rate of rotation tensor viewed in a moving reference frame with angular velocity ω_k. The constants A_0 and A_s are:

$A_0=4.04$ and $A_s=\sqrt{6}\cos\phi$
where:

$$\phi=\frac{1}{3}\cos^{-1}\left(\sqrt{6}\frac{S_{ij}S_{jk}S_{ik}}{S^3}\right)\Bigg|S=\sqrt{S_{ij}S_{ij}}$$

0.9 is found for the standard value of *Cμ* in the solution of equation of turbulent viscosity for an inertial sub layer in the equilibrium boundary layer. The model constant in this model are $C_{1\varepsilon}=1.44$, $C_{2\varepsilon}=1.9$, $\sigma_k=1.0$ while $\sigma_\varepsilon=1.2$ and C_1 can calculated by:

$$C_1=\max\left[0.43,\frac{\eta}{\eta+5}\right]\Bigg|_{\eta=\sqrt{2S_{ij}S_{ij}}\frac{k}{\varepsilon}} \tag{27}$$

2.2.4 Standard k-ω model

A Standard *k-ω* model was developed by Wilcox [26] in 1988. The Standard *k-ω* model was medicated for better calculation of low Reynolds number effects, compressibility and shear flow spreading. The free shear flow prediction in this model has a very good agreement in calculation of mixing layer, far wake and round, radial and plane jet. Hence, it is suitable to apply on wall-bounded flows and free shear flow. The free shear flow prediction in this model has a very good agreement in calculation of mixing layer, far wake and round, radial and plane jet. This Standard *k-ω* model governs the transport equations for turbulent kinetic energy and specific dissipation rate as show as:

$$\frac{\partial(\rho k)}{\partial t}+\frac{\partial(\rho k u_i)}{\partial x_i}=\frac{\partial}{\partial x_i}\left[\left(\mu+\frac{\mu_t}{\sigma_k}\right)\frac{\partial k}{\partial x_j}\right]+G_k-Y_k+S_k \tag{28}$$

$$\frac{\partial(\rho\omega)}{\partial t}+\frac{\partial(\rho\omega u_i)}{\partial x_i}=\frac{\partial}{\partial x_i}\left[\left(\mu+\frac{\mu_t}{\sigma_k}\right)\frac{\partial\omega}{\partial x_j}\right]+G_\omega-Y_\omega+S_\omega \tag{29}$$

where G_k is the generation of turbulent kinetic energy from the mean velocity gradient, G_ω is the generation of specific dissipation rate, Y_k is the dissipation of turbulent kinetic energy due to turbulence, Y_ω is the dissipation of k due to turbulence, S_k and S_ε are user sources term. σ_ω is the turbulent Prandtl number of specific dissipation rate and σ_k is the turbulent Prandtl number of the turbulent kinetic energy. The turbulent viscosity of Standard *k-ω* model is:

$$\mu_t=\alpha^*\frac{\rho k}{\omega} \tag{30}$$

A low Reynold number correction is caused from turbulent viscosity that damped by coefficient α^*. The coefficient α^* can be calculated by:

$$\alpha^*=\alpha_\infty^*\left(\frac{\alpha_0^*+\mathrm{Re}_t/\mathrm{Re}_k}{1+\mathrm{Re}_t/\mathrm{Re}_k}\right) \tag{31}$$

where:

$\mathrm{Re}_t=\frac{\rho k}{\omega}$, $\mathrm{R}_k=6$, $\alpha_0^*=\frac{\beta_i}{3}$, $\beta_i=0.072$

For high Reynold number of this model, $\alpha^*=\alpha_\infty^*=1$. The dissipation of *k and* ω, Y_k and Y_ω can be defined respectively as in Eqs. (32) and (33).

$$Y_k=\rho\beta^* f_\beta k\omega \tag{32}$$

$$Y_k=\rho\beta^* f_\beta\omega^2 \tag{33}$$

2.2.5 k-ω BSL model

k-ω BSL model was proposed by Menter [27] in 1994. This model combines the advantages of the *k-ε* model and *k-ω* model. This model effectively blends the robust and accurate formation of the *k-ω* model in the near wall region with the free-stream independence of the *k-ε* model in the far field. However, this model still fails to proper predict the onset and amount of flow separation from the smooth surfaces. Due to the both models do not account for transport of the turbulent shear stress, the overprediction of the eddy may occur. This *k-ω* BSL model governs the transport equations via the turbulent kinetic energy *k* and specific dissipation rate *ω* as shown in Eqs. (34) and (35).

$$\frac{\partial(\rho k)}{\partial t}+\frac{\partial(\rho k u_j)}{\partial x_j}=\frac{\partial}{\partial x_j}\left[(\mu+\sigma_k\mu_t)\frac{\partial k}{\partial x_j}\right]+P+\beta^*\rho\omega k \tag{34}$$

$$\frac{\partial(\rho\omega)}{\partial t}+\frac{\partial(\rho\omega u_j)}{\partial x_j}=\frac{\partial}{\partial x_j}\left[(\mu+\sigma_\omega\mu_t)\frac{\partial\omega}{\partial x_j}\right]+\frac{\gamma}{v_t}P+\beta^*\rho\omega^2+2(1-F_1)\frac{\rho\sigma_{\omega 2}}{\omega}\frac{\partial k}{\partial x_j}\frac{\partial\omega}{\partial x_j} \tag{35}$$

where:

$$P = \tau_{ij} \frac{\partial u_i}{\partial x_j} \tag{36}$$

$$F_1 = \tan\left\{\left[\min\left[\max\left(\frac{2\sqrt{k}}{0.09\omega y'}, \frac{500}{y^2\omega}\right), \frac{4\rho\sigma_{\omega 2}}{CD_{k\omega}y^2}\right]\right]^4\right\} \tag{37}$$

where

$$\mu_t = \frac{\rho k}{\omega} \tag{38}$$

$$CD_{k\omega} = \max\left(2\rho\sigma_{\omega 2}\frac{1}{\omega}\frac{\partial k}{\partial x_j}\frac{\partial \omega}{\partial x_j}, 10^{-20}\right) \tag{39}$$

The coefficient of β, γ, σ_k and σ_ω are computed as:

$$\left.\begin{aligned} \beta &= F_1\beta_1 + (1+F_1)\beta_2 \\ \gamma &= F_1\gamma_1 + (1+F_1)\gamma_2 \\ \sigma_k &= F_1\sigma_{k1} + (1+F_1)\sigma_{k2} \\ \sigma_\omega &= F_1\sigma_{\omega 1} + (1+F_1)\sigma_{\omega 2} \end{aligned}\right\} \tag{40}$$

the model constants are: β^* = 0.09, β_1 = 0.075, β_2 = 0.0828, $\gamma_1 = \beta_1/\beta^*$, $\gamma_2 = \beta_2/\beta^*$, σ_{k1} = 0.5, σ_{k2} = 1.5, $\sigma_{\omega 1}$ = 0.5 and $\sigma_{\omega 1}$ = 0.856.

2.2.6 k-ω SST model

k-ω SST model is modified model from standard k-ω model. The *k-ω* SST model was developed by Menter [28] too in 1993. This model effectively blends the robust and accurate formation of the k-ω model in the near wall region with the free-stream independence of the *k-ε* model in the far field. By these features, the *k-ω* SST model is more reliable and accurate for a wider class of flows. This model also can be perceived as a combination of *k-ε* model and *k-ω* model. This model was developed to overcome the problem of overprediction in *k-ω* BSL model. This *k-ω* SST model governs the transport equations via the turbulent kinetic energy and specific dissipation rate as show below.

$$\frac{\partial(\rho k)}{\partial t} + \frac{\partial(\rho k u_i)}{\partial x_i} = \frac{\partial}{\partial x_i}\left[\left(\mu + \frac{\mu_t}{\sigma_k}\right)\frac{\partial k}{\partial x_j}\right] + G_k - Y_k + S_k \tag{41}$$

$$\frac{\partial(\rho\omega)}{\partial t} + \frac{\partial(\rho\omega u_i)}{\partial x_i} = \frac{\partial}{\partial x_i}\left[\left(\mu + \frac{\mu_t}{\sigma_\omega}\right)\frac{\partial k}{\partial x_j}\right] + G_\omega - Y_\omega + D_\omega + S_\omega \tag{42}$$

where G_k is the generation of turbulent kinetic energy from the mean velocity gradient, G_ω is the generation of specific dissipation rate, Y_k is the dissipation of turbulent kinetic energy due to turbulence, Y_ω is the dissipation of k due to turbulence, S_k and S_ε are user sources term. σ_ω is the turbulent Prandtl number of specific dissipation rate and σ_k is the turbulent Prandtl number of the turbulent kinetic energy. The turbulent viscosity is:

$$\mu_t = \frac{\rho k}{\omega A}\left| A = \max\left(\frac{1}{\alpha'}, \frac{SF_2}{a_1 \omega}\right)\right. \tag{43}$$

The σ_k and σ_ω are given by:

$$\sigma_k = \frac{1}{F_1 / \sigma_{k,1} + (1 - F_1) / \sigma_{k,2}} \tag{44}$$

$$\sigma_\omega = \frac{1}{F_1 / \sigma_{\omega,1} + (1 - F_1) / \sigma_{\omega,2}} \tag{45}$$

The blending function F_1 and F_2 are:

$$F_1 = \tanh\left(\Phi_1^4\right) \tag{46}$$

$$F_2 = \tanh\left(\Phi_2^2\right) \tag{47}$$

where:

$$\Phi_1 = \min\left[\max\left(\frac{\sqrt{k}}{0.09\omega y}, \frac{500\mu}{\rho y^2 \omega}\right), \frac{4\rho k}{\sigma_{\omega,2} D_\omega^+ y^2}\right] \tag{48}$$

$$D_\omega^+ = \max\left(2\rho \frac{1}{\sigma_{\omega,2}} \frac{1}{\omega} \frac{\partial k}{\partial x_j} \frac{\partial \omega}{\partial x_j}, 10^{-10}\right) \tag{49}$$

$$\Phi_2 = \max\left(\frac{2\sqrt{k}}{0.09\omega y}, \frac{500\mu}{\rho y^2 \omega}\right) \tag{50}$$

The Y_k and Y_ω are defined as:

$$\gamma_k = \rho \beta^* k \omega \tag{51}$$

$$\gamma_\omega = \rho \beta^* \omega^2 \tag{52}$$

The model constants are: $\beta_{i,1}$ = 0.075, $\beta_{i,2}$ = 0.0828, $\sigma_{k,1}$ = 1.176, $\sigma_{k,2}$ = 1.0, $\sigma_{\omega,1}$ = 2.0 while $\sigma_{\omega,2}$ = 1.168.

2.2.7 Computational method

In this study, 3×10^6 Reynolds number flow across two-dimensional NACA 0012 airfoil is simulated by using ANSYS Fluent version 17.0 at various angle of attack (-12° to 20°). C-type topology was decided to use in simulation because the structured quadrilateral element had the advantages of a higher degree of control and accuracy, lower memory consumption and a faster convergence rate. Thus, it can minimize the skewness of a near wall mesh. The residual setting is set to 0.0001. The domain height was set to 20 chord length and the domain length was set to 30 chord length. The airfoil was located at the centre of the semicircle. According to Yao *et al.,* [29], the grid cells were sufficient when the number of grids is above 80000. Thus, total 104000 quadrilateral cells were applied in the mesh generation. The Figure 1 showed the mesh of the computational domain around NACA 0012.

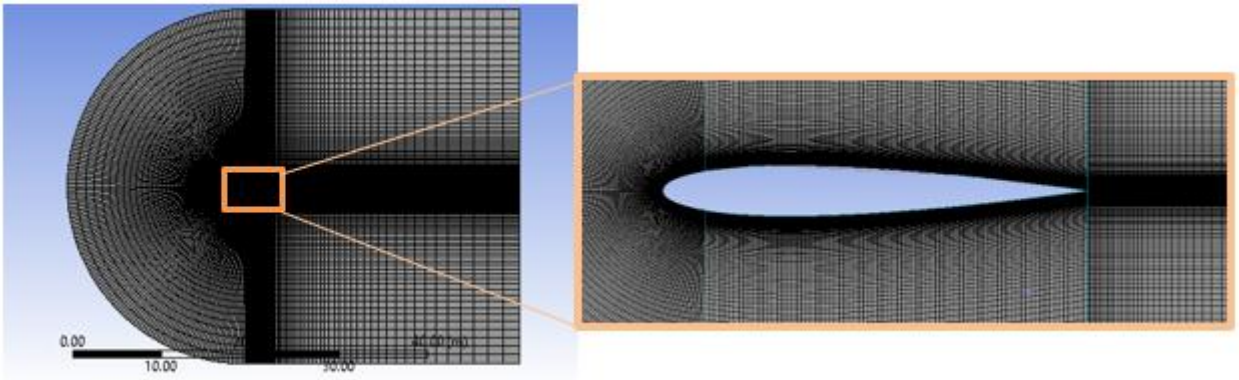

Fig. 1. Mesh of the computational domain around NACA 0012

The inlet boundary condition is set to 5% turbulence intensity of velocity inlet. However, the outlet boundary condition is set to 5% turbulence intensity of pressure outlet. No slip wall boundary condition is set on the airfoil surface. SIMPLEC algorithm is used to solve the pressure-velocity coupling in momentum equation and momentum, turbulence kinetic energy and dissipation ratio. Second-order upwind model is applied for discretisation of convection term due to its accuracy in calculation [30]. The numerical detail that used in simulation is summarised as Table 1.

Table 1
Numerical detail for simulation on flow across NACA 0012 airfoil

Input	Value
Reynold number	$3x10^6$
Operating temperature	300 K
Density of fluids	$1.225kg/m^3$
Viscosity of fluids	$1.7894x10^{-5}kg/ms$
Flow velocity	44 m/s
Chord length	1 m
Angle of attack	-12° to 20°

3. Results and Discussion

3.1 Lift and Drag Coefficient

A graph of lift coefficient versus angle of attack was plotted as shown as Figure 2 while a graph of drag coefficient versus angle of attack was plotted as shown as Figure 3. By observing the graph in Figure 2, the experimental curve can be noticed that the lift coefficient increases linearly while

increasing the angle of attack at low angle of attack which is in the range of -12° to 15°. In -9° to 9° of angle of attack, all turbulence models show a very good agreement with the experimental data for lift coefficient [31]. All the turbulence models also increased linearly from -10° to 10° which similar to experimental data. After 12° angle of attack, all the turbulence model started to have some different with experimental data. However, the standard *k-Ω* model had the lowest deviation with experimental data compared to other turbulence models while the flow starts to separate. At higher angle of attack, the upper surface flow of the airfoil began to separate. The flow no longer follows along the airfoil surface. This is a region above the upper surface and near the airfoil trailing edge. In this region, the velocity is low and the flow reverses in place in a turbulence motion. This separation flow is known as trailing edge separation [29].

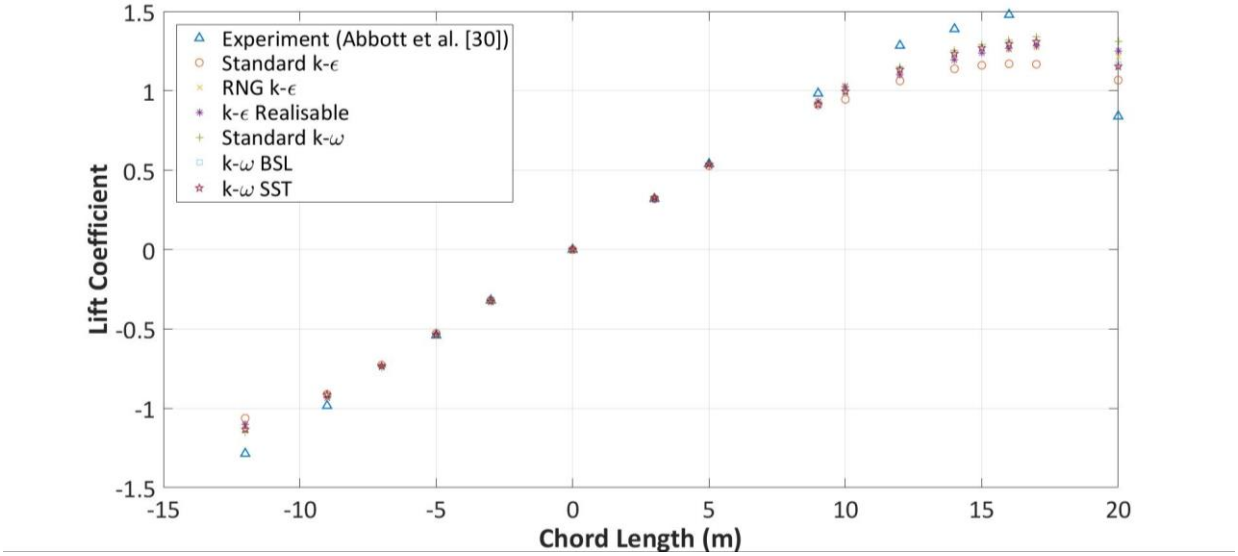

Fig. 2. Comparison graph of lift coefficient versus angle of attack between experimental data from [31] and simulation result of turbulence models for NACA 0012 airfoil

As the angle of attack is increased further, the separation flow region continuous moves toward the leading edge. At certain critical angle of attack, the lift coefficient will drop rapidly and drag coefficient will increase rapidly. This condition was called stall and the angle of attack where the stall begin was known as stall angle. This condition is called stall and the critical angle of attack is called stall angle. In the stall angle, the airfoil will have a maximum lift coefficient [32]. The four turbulence models were noticed that the stall angle is around 16° to 17° by observing both Figure 2 and 3. Around the stall angle, the standard *k-Ω* is closer to the experimental data.

For drag coefficient, all the turbulence models overpredict the drag coefficient by observing Figure 3. However, all the turbulence models still get the same shape of curve with the experimental data. By comparing the turbulence models with the experimental data, the standard *k-ω* show the best agreement with experimental data in drag coefficient curve. The overprediction of the drag coefficient may be caused by the sensitivity of drag coefficient to the roughness of surface [33]. Indeed, the real airfoil has laminar flow over the forward half. The turbulence models are unable to calculate the transition point between laminar and turbulent. The models just consider that the boundary layer is turbulent along the chord length. However, in theory, the turbulence boundary layer will carry more energy. Thus, the drag coefficient is much higher than the viscous boundary layer. By observing and comparing the curses in drag coefficient, the *k-ω* SST model is found to have a better agreement with experimental data, in accordance with the conclusion drawn by Jehad *et al.,* [34].

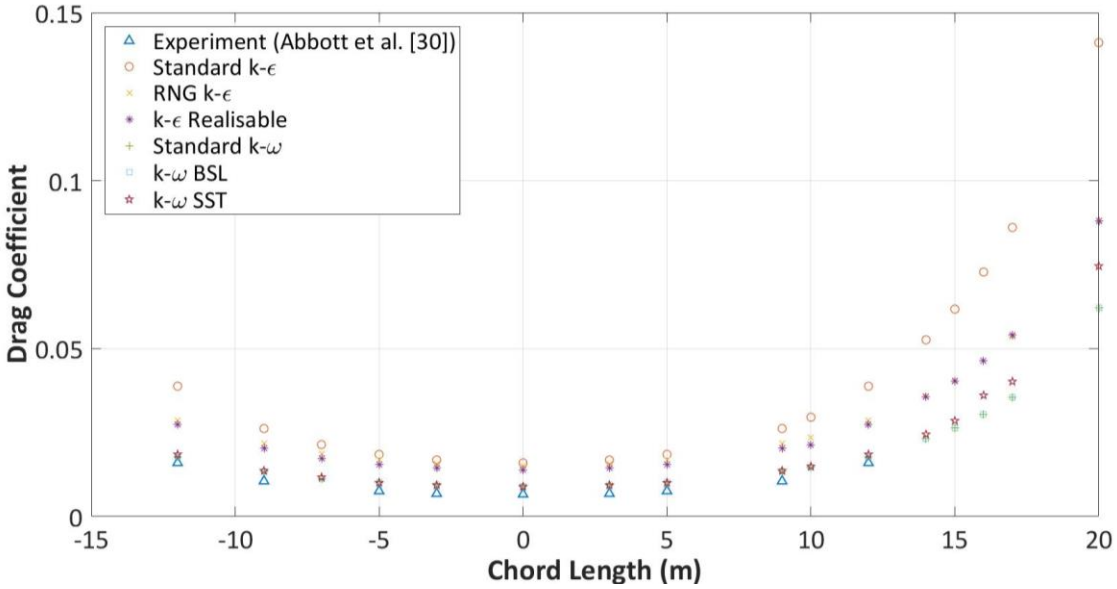

Fig. 3. Comparison graph of drag coefficient versus angle of attack between experimental data from [31] and simulation result of turbulence models for NACA 0012 airfoil

A chart of Root Mean Square Error of drag coefficient and lift coefficient in four different turbulence models for NACA 0012 was plotted as shown as Figure 4. By comparing the root mean square error in lift coefficient, k-ω SST model is noticed that have the lowest root mean square error among the models. However, k-ω BSL model is found that have the lowest root mean square error in drag coefficient model. In overall comparison in lift and drag coefficient, k-ω SST model should be the best model among the four model. The k-ω SST model have a lowest root mean square error in lift coefficient and second lowest root mean square error in drag coefficient. Thus, the k-ω SST model can predict the most accurate lift coefficient and acceptable drag coefficient among the four turbulence models in NACA 0012.

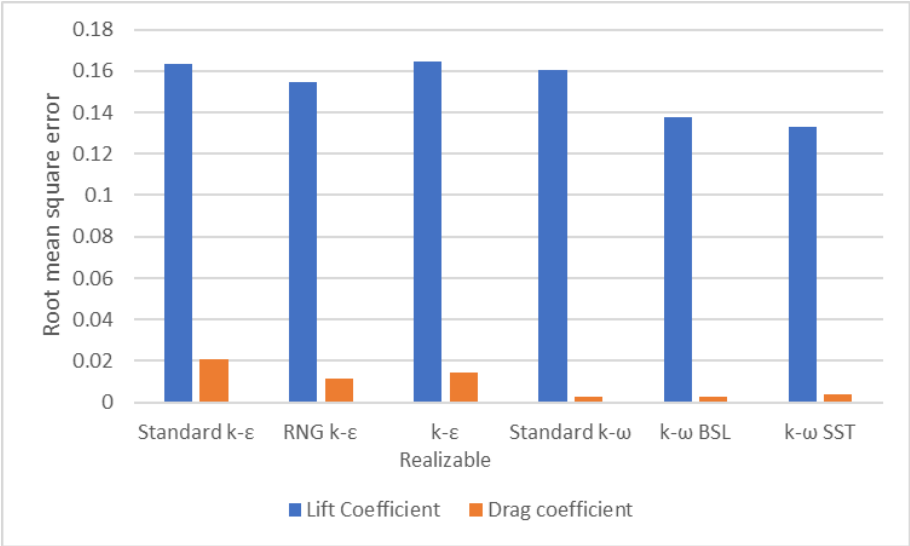

Fig. 4. Chart of Root Mean Square Error of drag coefficient and lift coefficient in different turbulence models for NACA 0012

3.2 Pressure Coefficient

The distribution of pressure coefficient on NACA 0012 airfoil at different angle of attack in different turbulence models are shown as Figures 5 to 11. However, the experimental data [33] of distribution of pressure coefficient on NACA 0012 airfoil at 0°, 10° and 15° angle of attack in four turbulence models was shown as Figures 7, 9 and 10. By comparing the different turbulence model result, it showed that all the turbulence models had almost same curve with each other but standard *k-ε* shown small deviation with other turbulence models at lower and higher angle of attack (-12°, 12° and 20°). Moreover, the *k-ε* Realizable model also shown small deviation with other turbulence models at 20° angle of attack. By comparing the simulation result with the experimental data, the turbulence models showed a very good agreement with the experimental data.

While the angle of attack was less than zero, the pressure coefficient of upper surface was positive and lower surface was negative. This showed that lift force pointed below while the angle of attack was negative or less than zero. However, the pressure coefficient of upper was negative and lower surface was positive when the angle is more than zero. This showed that lift force pointed upward while the angle of attack was positive or more than zero. By observing the result, it can be noticed that the leading edge had a larger curvature. This showed that the flow on the surface had a large acceleration and lower static pressure on the surface. It also can be seen that the angle of attack between -10° to 10° had obvious inclination at the trailing edge. While the angle of attack was closing to zero, the inclination was increased. This was an anti-curvature section on the trailing edge. In this section, the velocity was lower and the pressure was increased. From the result, it also can be noticed that while the angle of attack was increased from 0° to 20° or decreased from 0° to -12°, the difference of pressure coefficient between upper and lower surface at leading edge was increased. This showed that when the difference of pressure coefficient between upper and lower surface at leading edge was higher, the lift force mostly come from leading edge.

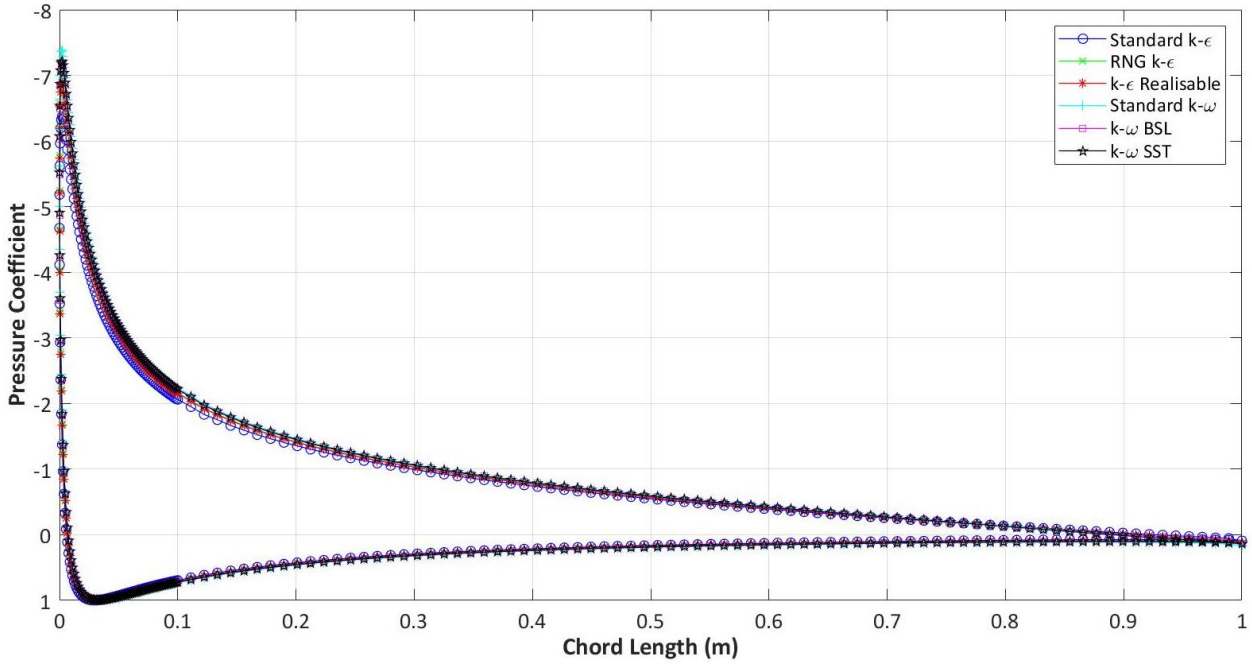

Fig. 5. Graph of pressure coefficient against airfoil position for four different turbulence models at -12° angle of attack on NACA 0012

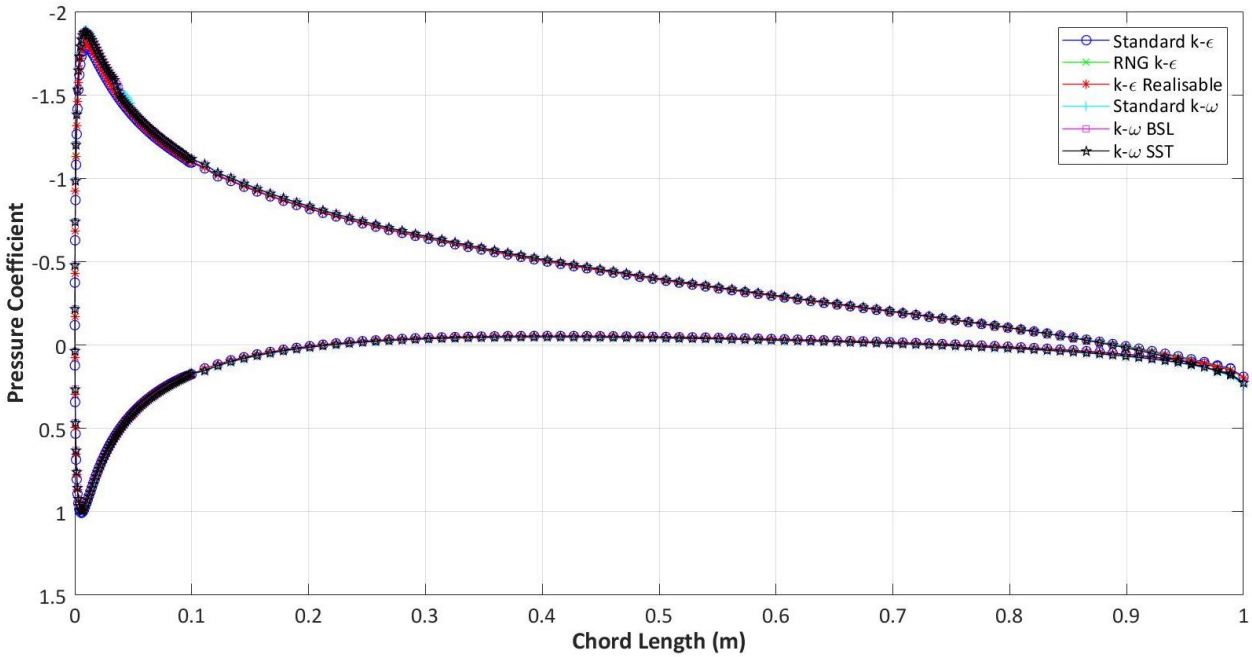

Fig. 6. Graph of pressure coefficient against airfoil position for four different turbulence models at -5° angle of attack on NACA 0012

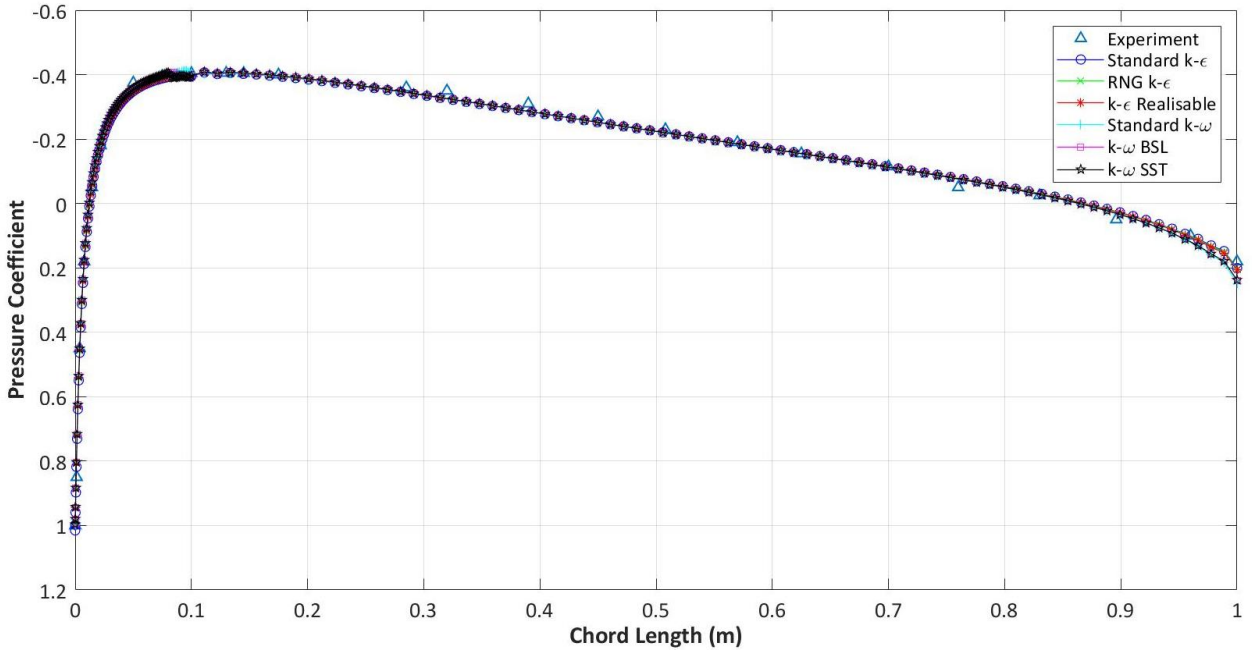

Fig. 7. Graph of pressure coefficient against airfoil position for four different turbulence models at 0° angle of attack on NACA 0012

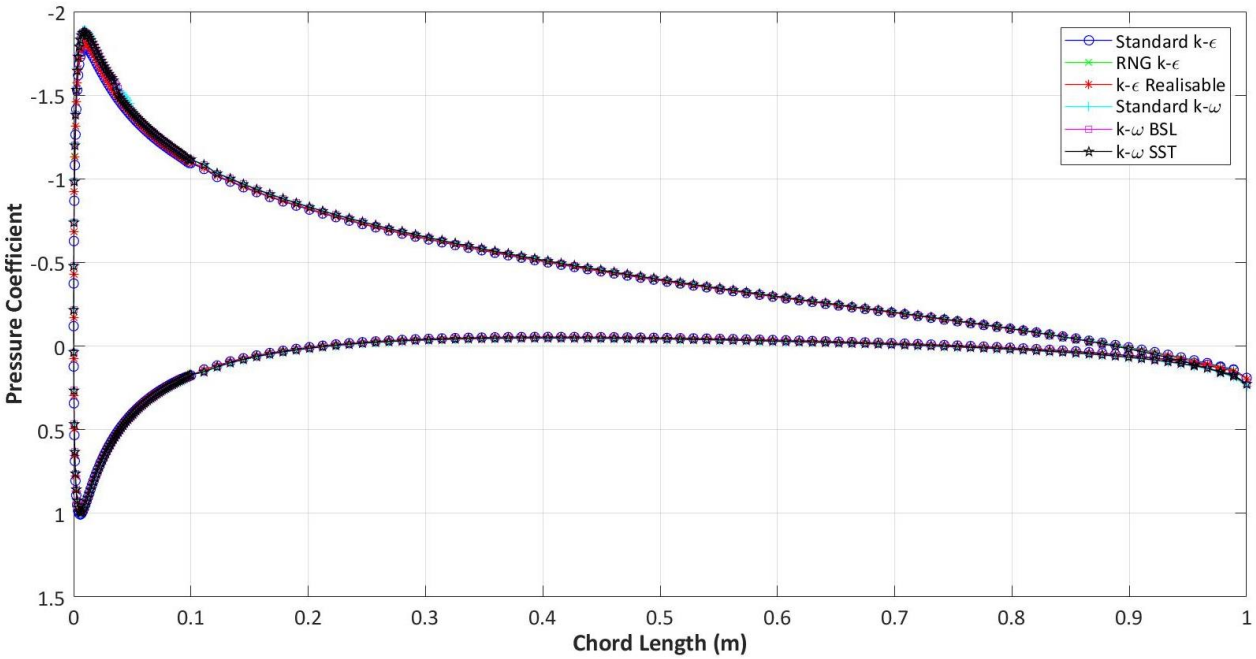

Fig. 8. Graph of pressure coefficient against airfoil position for four different turbulence models at 5° angle of attack on NACA 0012

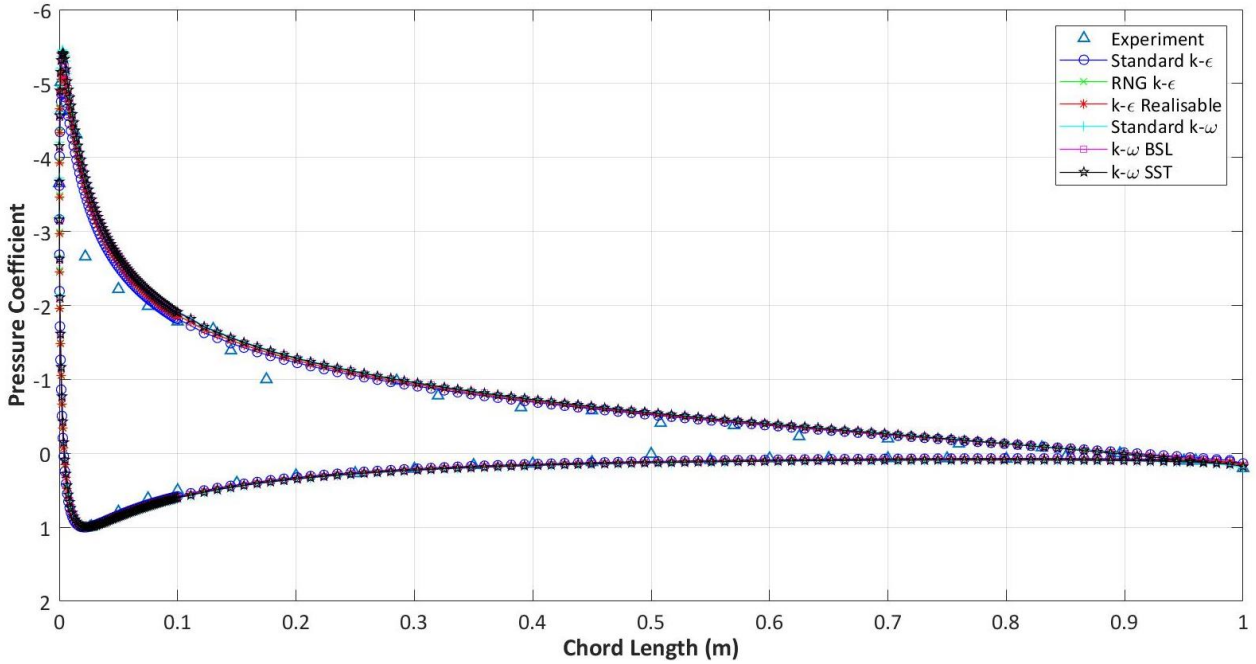

Fig. 9. Graph of pressure coefficient against airfoil position for four different turbulence models at 10° angle of attack on NACA 0012

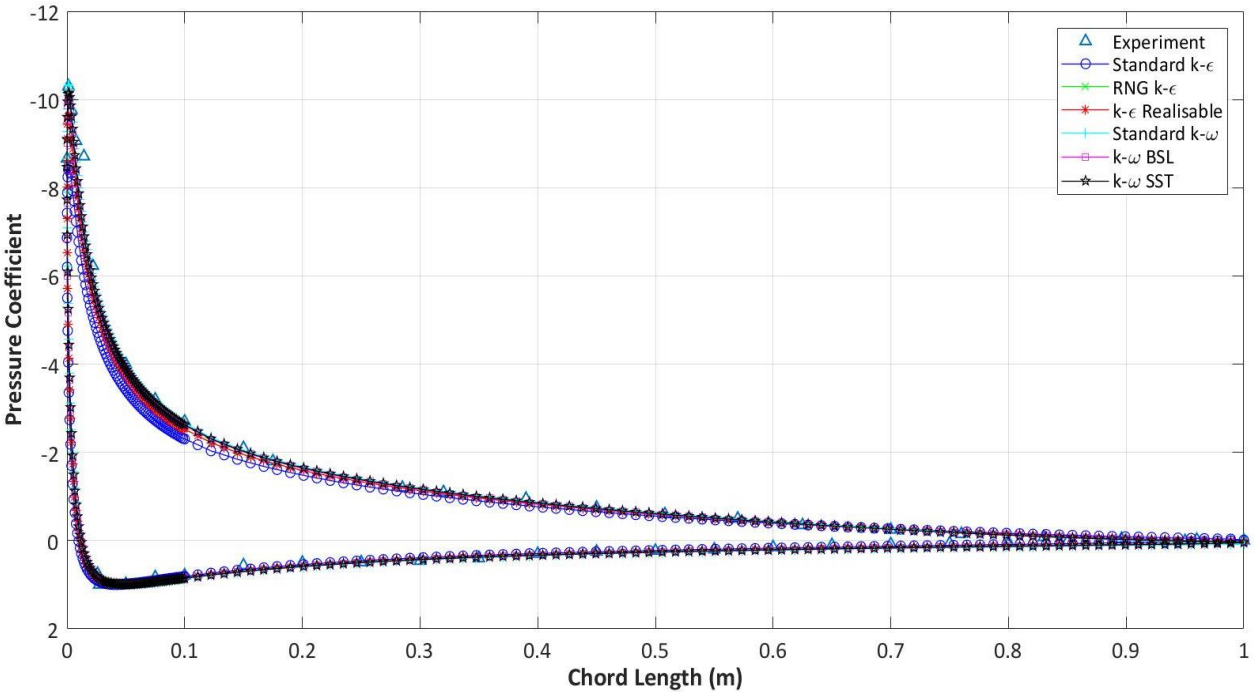

Fig. 10. Graph of pressure coefficient against airfoil position for four different turbulence models at 15° angle of attack on NACA 0012

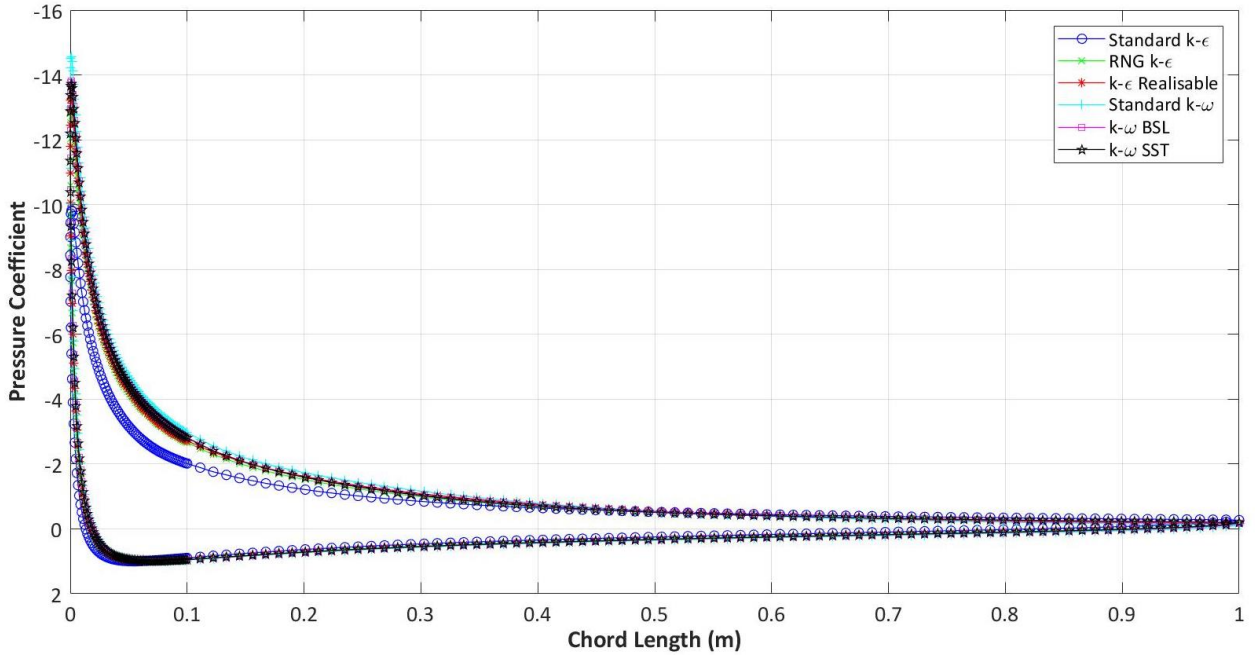

Fig. 11. Graph of pressure coefficient against airfoil position for four different turbulence models at 20° angle of attack on NACA 0012

3.3 Contours of Static Pressure and Velocity Magnitude

The general flow pattern of the flow across NACA 0012 is discussed here by taking the simulation results by RNG *k-ε* model as example. Figure 12 showed contours of static pressure across NACA 0012 at -12° to 20° angle of attack. In addition, Figure 13 showed contours of velocity magnitude across NACA 0012 at -12° to 20° angle of attack.

At 0^o angle of attack, the static pressure across NACA 0012 were symmetric. Thus, the lift force was zero in this angle of attack. The stagnation point also was noticed that located exactly at the nose of the airfoil. The maximum pressure and zero velocity occurred at the stagnation point. While the angle of attack increase in positive or negative, the static pressure across airfoil became non-symmetric. As the angle of attack increase from 0^o to 20^o, the pressure on lower surface became higher than the pressure on upper surface according to Bernoulli's principle. The imbalance of pressure caused the lift force in upward direction on airfoil. However, while the angle of attack increase in negative, the lift force was negative due to the higher static pressure on upper surface. By the contours, low velocity can be observed in high pressure region. Moreover, when the angle of attack increases positively from zero angle, the stagnation point is moved toward the trailing edge on the bottom surface. In opposite, the stagnation point is moved toward the trailing edge on the upper surface as the angle of attack increase in negative from zero angle. Thus, the lift coefficient will continue increase with angle of attack until maximum in stall angle then start to decrease. As the angle of attack up to about 12^o, the boundary layer still fully attached the airfoil. However, if the angle of attack further increases from 10^o, the boundary layer is thickened from the trailing edge and move toward leading edge direction. Thus, the boundary layer separation is started to occur. In the end, lift force will decrease obviously and drag force increase rapidly. This condition also known as stall.

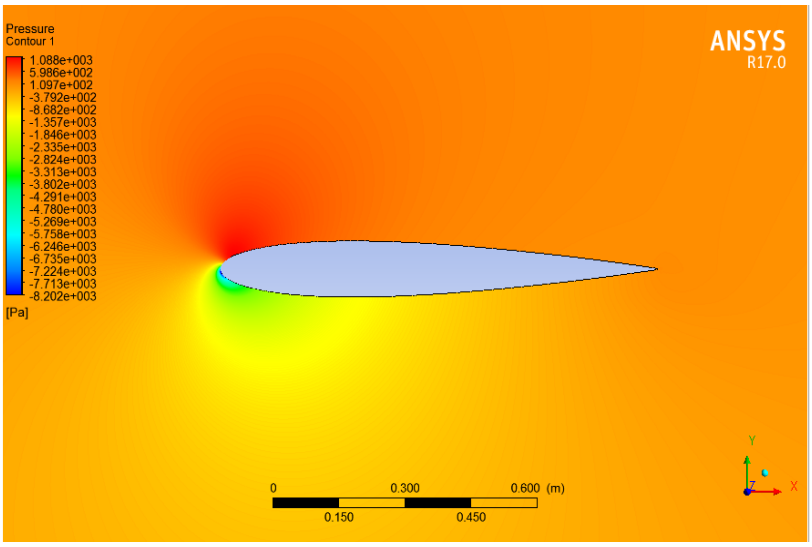

(a)

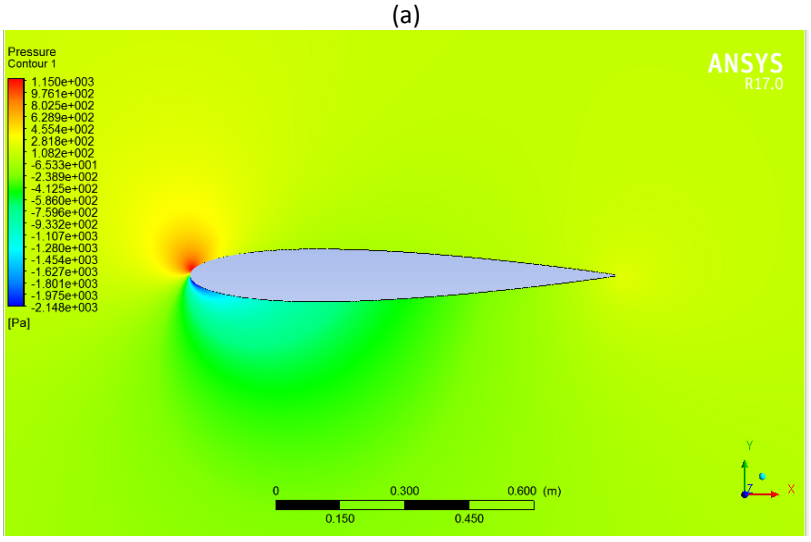

(b)

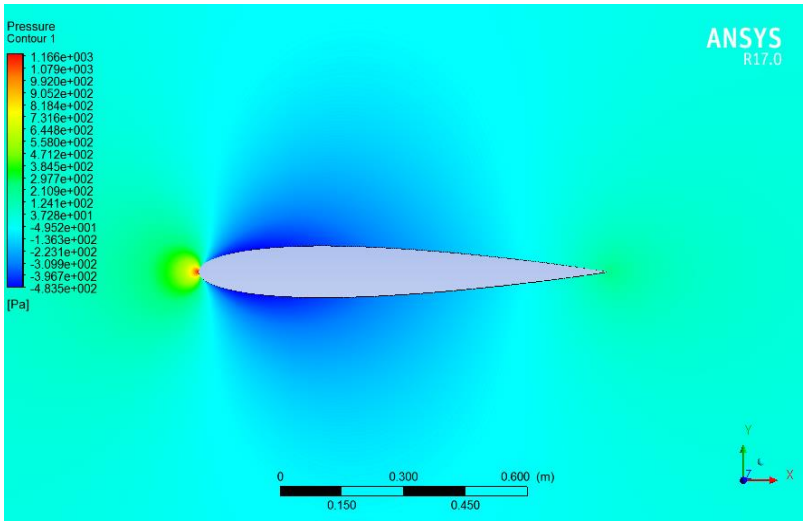
Pressure
Contour 1
1.166e+003
1.079e+003
9.920e+002
9.052e+002
8.184e+002
7.316e+002
6.448e+002
5.580e+002
4.712e+002
3.845e+002
2.977e+002
2.109e+002
1.241e+002
3.728e+001
-4.952e+001
-1.363e+002
-2.231e+002
-3.099e+002
-3.967e+002
-4.835e+002
[Pa]
ANSYS
R17.0
0
0.300
0.600 (m)
0.150
0.450
Y
Z
X

(c)

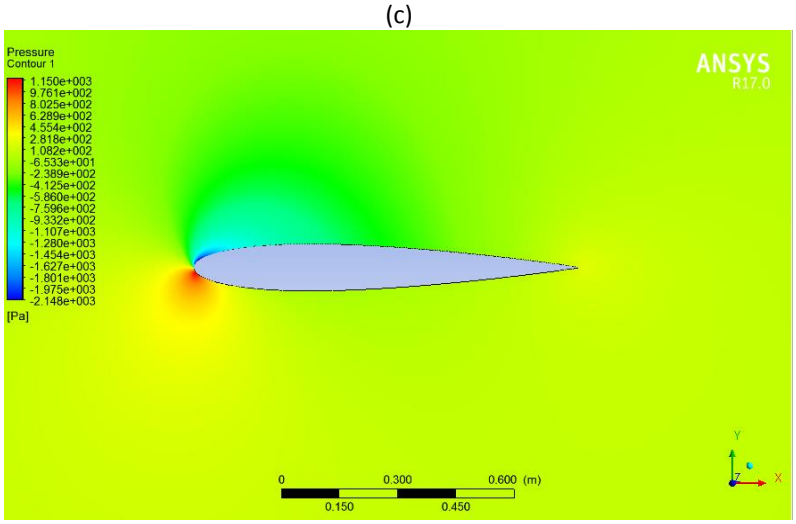
Pressure
Contour 1
1.150e+003
9.761e+002
8.025e+002
6.289e+002
4.554e+002
2.818e+002
1.082e+002
-6.533e+001
-2.389e+002
-4.125e+002
-5.860e+002
-7.596e+002
-9.332e+002
-1.107e+003
-1.280e+003
-1.454e+003
-1.627e+003
-1.801e+003
-1.975e+003
-2.148e+003
[Pa]
ANSYS
R17.0
0
0.300
0.600 (m)
0.150
0.450
Y
Z
X

(d)

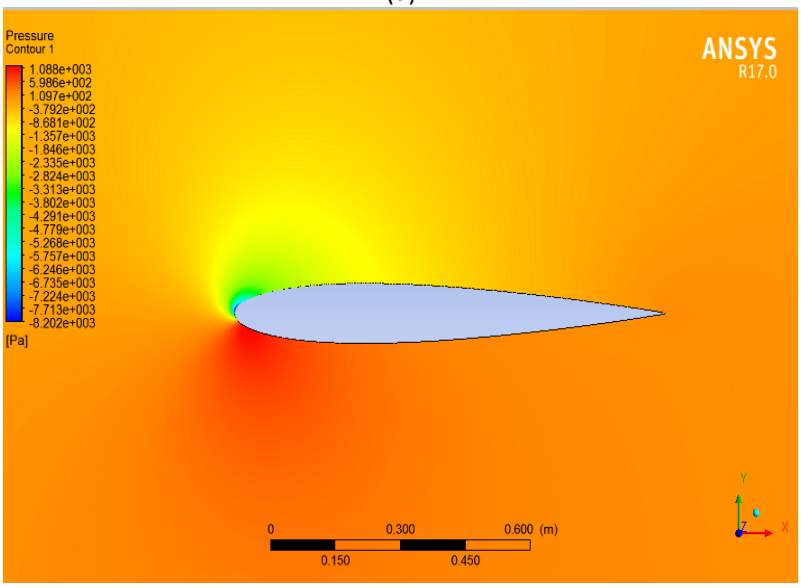
Pressure
Contour 1
1.088e+003
5.986e+002
1.097e+002
-3.792e+002
-8.681e+002
-1.357e+003
-1.846e+003
-2.335e+003
-2.824e+003
-3.313e+003
-3.802e+003
-4.291e+003
-4.779e+003
-5.268e+003
-5.757e+003
-6.246e+003
-6.735e+003
-7.224e+003
-7.713e+003
-8.202e+003
[Pa]
ANSYS
R17.0
0
0.300
0.600 (m)
0.150
0.450
Y
Z
X

(e)

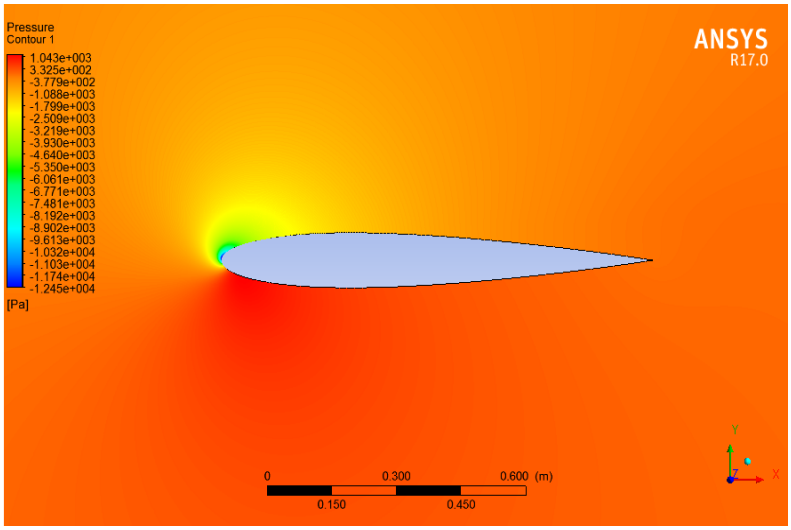

(f)

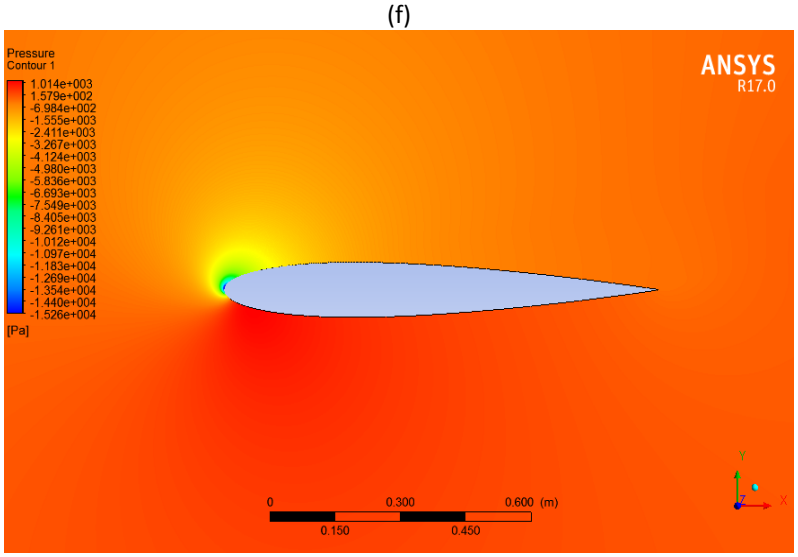

(g)

Fig. 12. Contours of static pressure across NACA 0012 at (a) -12°, (b) -5°, (c) 0°, (d) 5°, (e) 12° and (f) 16° and (g) 20°

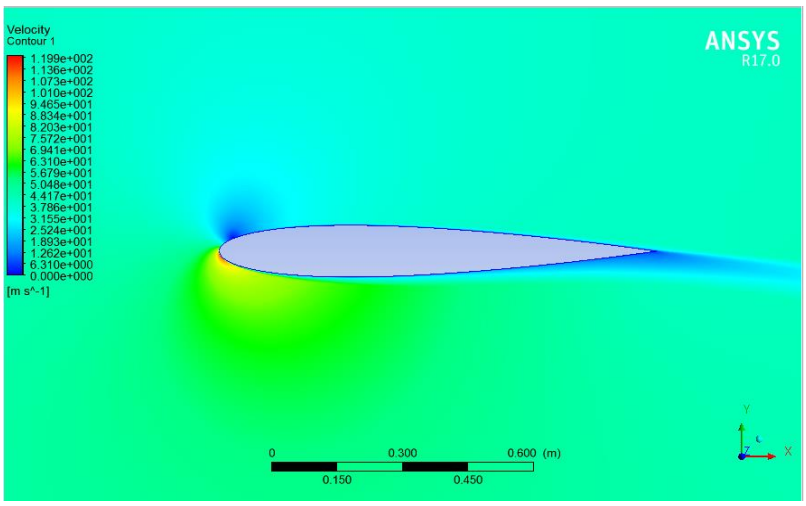

(a)

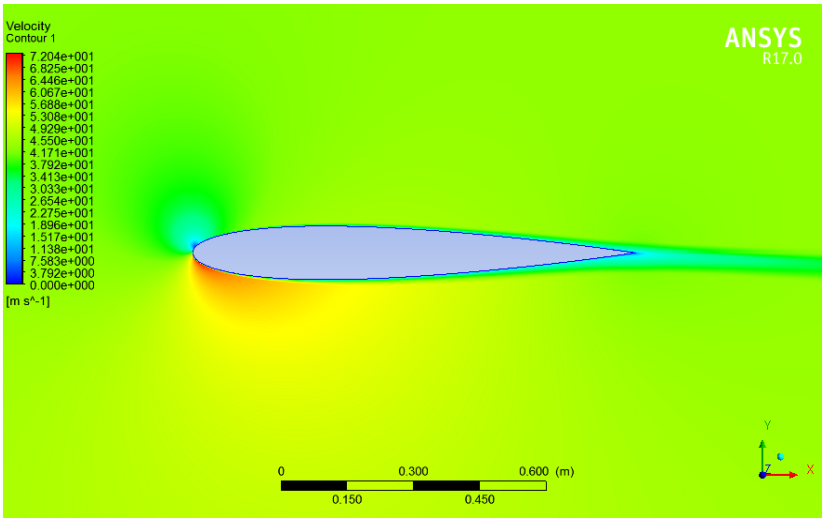
Velocity
Contour 1
7.204e+001
6.825e+001
6.446e+001
6.067e+001
5.688e+001
5.308e+001
4.929e+001
4.550e+001
4.171e+001
3.792e+001
3.413e+001
3.033e+001
2.654e+001
2.275e+001
1.896e+001
1.517e+001
1.138e+001
7.583e+000
3.792e+000
0.000e+000
[m s^-1]
ANSYS
R17.0
0
0.300
0.600 (m)
0.150
0.450
Y
Z
X

(b)

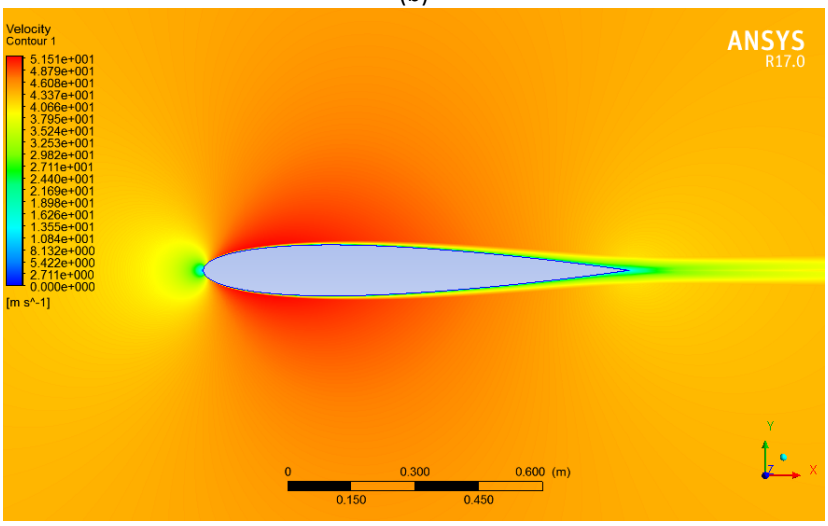
Velocity
Contour 1
5.151e+001
4.879e+001
4.608e+001
4.337e+001
4.066e+001
3.795e+001
3.524e+001
3.253e+001
2.982e+001
2.711e+001
2.440e+001
2.169e+001
1.898e+001
1.626e+001
1.355e+001
1.084e+001
8.132e+000
5.422e+000
2.711e+000
0.000e+000
[m s^-1]
ANSYS
R17.0
0
0.300
0.600 (m)
0.150
0.450
Y
Z
X

(c)

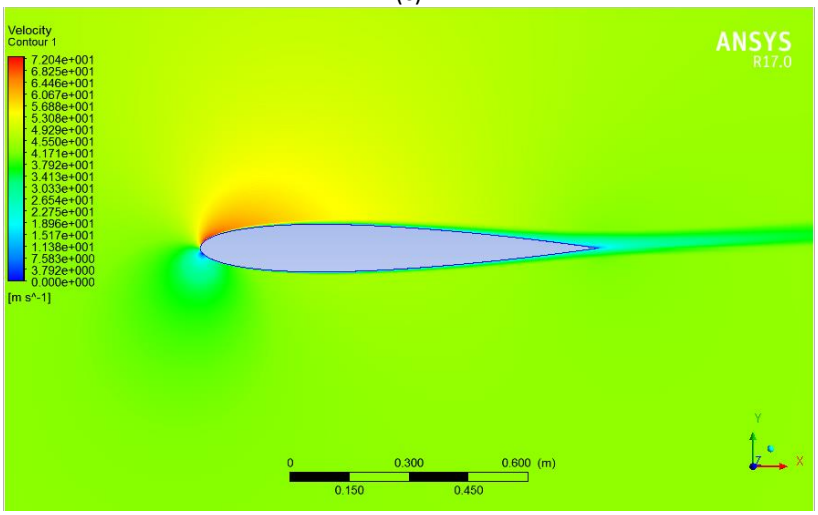
Velocity
Contour 1
7.204e+001
6.825e+001
6.446e+001
6.067e+001
5.688e+001
5.308e+001
4.929e+001
4.550e+001
4.171e+001
3.792e+001
3.413e+001
3.033e+001
2.654e+001
2.275e+001
1.896e+001
1.517e+001
1.138e+001
7.583e+000
3.792e+000
0.000e+000
[m s^-1]
ANSYS
R17.0
0
0.300
0.600 (m)
0.150
0.450
Y
Z
X

(d)

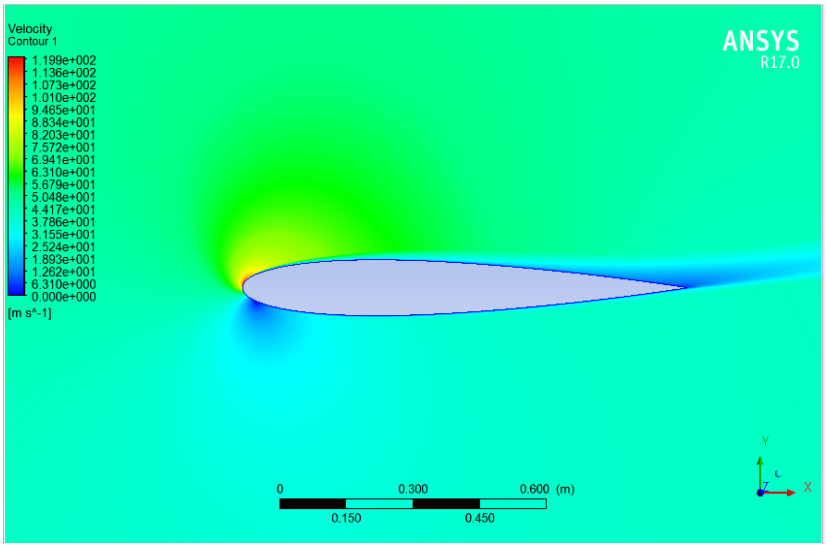

(e)

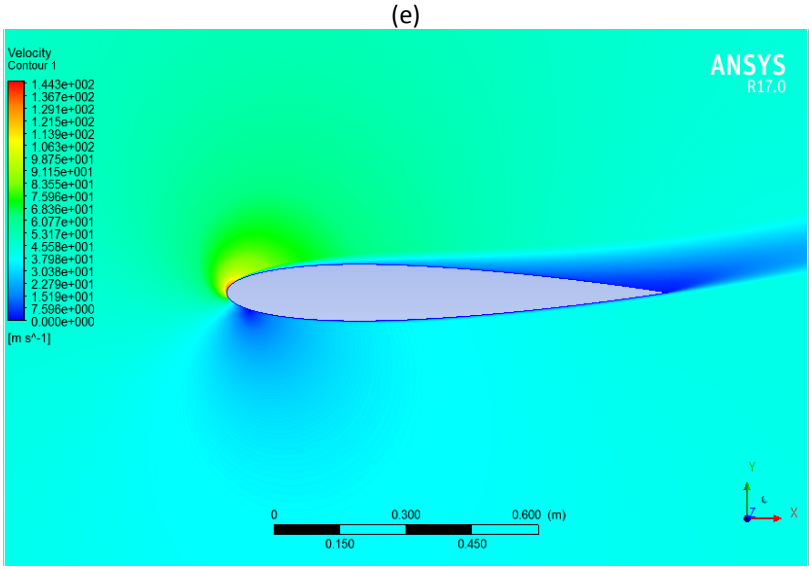

(f)

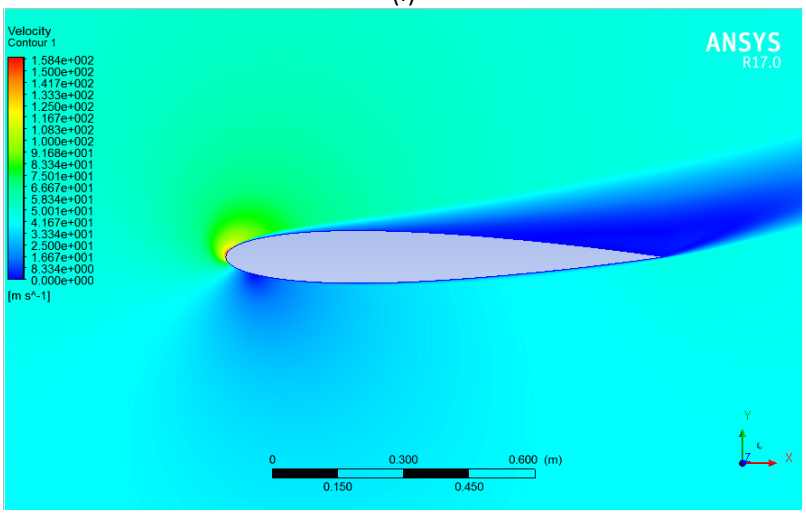

(g)

Fig. 13. Contours of velocity across NACA 0012 at (a) -12°, (b) -5°, (c) 0°, (d) 5°, (e) 12° and (f) 16° and (g) 20°

3.4 Convergence Rate

Table 2 was tabulated to show number of iterations until 0.0001 for the turbulence model at 0° angle of attack. By the result, RNG *k-ε* had the lowest convergence rate among all turbulence model.

Table 2
Convergence rate for four different turbulence models

Turbulence model	Number of literation
Standard *k-ε*	847
RNG *k-ε*	953
k-ε Realizable	869
Standard *k-ω*	390
k-ω BSL	616
k-ω SST	568

4. Conclusions

In this study, the flow across NACA 0012 airfoil is studied in various angle of attack which is -12° to 20° by using four different two-equation turbulence models in ANSYS Fluent R17. The two-equation turbulence models that used in the study are standard *k-ε* model, RNG *k-ε* model, *k-ε* Realizable model, standard *k-ω* model, *k-ω* BSL model and *k-ω* SST model. It is aiming to analyse the velocity and pressure field around NACA 0012 airfoil in different angle of attack. Moreover, lift, drag and pressure coefficient are also analysed in different angle of attack and compared to experimental data. The convergence rate of two-equation turbulence models is compared in this study.

For lift coefficient result, *k-ω* SST model showed the best agreement with the experimental result among other turbulence models. However, the *k-ω* BSL model showed the best agreement with experimental result in drag coefficient among other turbulence models. However, the *k-ω* SST model has a best result in overall. It can get the best result in lift coefficient and acceptable result in drag coefficient. The predicted drag coefficients of the turbulence models are higher than the experimental data. This overprediction is occurred because the actual airfoil has laminar flow over forward half. In overall, RNG *k-ε* model is noticed that is a most suitable turbulence model to study flow across NACA 0012 as it gets a best result in lift coefficient and second upper good result in drag coefficient.

In pressure coefficient result, it showed that all the turbulence models had almost same curve with each other but Standard *k-ε* shown small deviation with other turbulence models at lower and higher angle of attack (-12°, 12° and 20°). By comparing the simulation result with the experimental data, the turbulence models showed a very good agreement with the experimental data.

In comparison of convergence rate, *k-ω* SST model showed the lower convergence rate. Thus, *k-ω* SST model should be the best turbulence model in this study. The drag and lift coefficient result also showed the *k-ω* SST model is the most suitable turbulence model in overall.

Acknowledgement
The authors would like to thank the support from Takasago Research Fund (Vote No: 4B314) from Malaysia-Japan International Institute of Technology, Universiti Teknologi Malaysia and the Pioneer Scientist Incentive Fund (PSIF) with vote number Proj-In-FETBE-038.

References

[1] Schiestel, Roland. *Modeling and simulation of turbulent flows*. Vol. 4. John Wiley & Sons, 2010.
[2] Pyakurel, Parakram, James H. VanZwieten, Manhar Dhanak, and Nikolaos I. Xiros. "Numerical modeling of turbulence and its effect on ocean current turbines." *International journal of marine energy* 17 (2017): 84-97.
[3] Anup, K. C., Jonathan Whale, Samuel P. Evans, and Philip D. Clausen. "An investigation of the impact of wind speed and turbulence on small wind turbine operation and fatigue loads." *Renewable Energy* 146 (2020): 87-98.
[4] Zhang, T., Y. O. Zhang, and H. Ouyang. "Structural vibration and fluid-borne noise induced by turbulent flow through a 90 piping elbow with/without a guide vane." *International Journal of Pressure Vessels and Piping* 125 (2015): 66-77.
[5] Bryant, D. B., Ephraim M. Sparrow, and John M. Gorman. "Turbulent pipe flow in the presence of centerline velocity overshoot and wall-shear undershoot." *International Journal of Thermal Sciences* 125 (2018): 218-230.
[6] Liu, Haidong, Deqi Chen, Lian Hu, Dewen Yuan, and Hong Gao. "Numerical investigations on flow-induced vibration of fuel rods with spacer grids subjected to turbulent flow." *Nuclear Engineering and Design* 325 (2017): 68-77.
[7] Quen, Lee Kee, Aminudin Abu, Naomi Kato, Pauziah Muhamad, Lit Ken Tan, and Hooi Siang Kang. "Performance of two-and three-start helical strakes in suppressing the vortex-induced vibration of a low mass ratio flexible cylinder." *Ocean Engineering* 166 (2018): 253-261.
[8] Zambra, C. E., C. Rosales, N. O. Moraga, and M. Ragazzi. "Self-heating in a bioreactor: Coupling of heat and mass transfer with turbulent convection." *International Journal of Heat and Mass Transfer* 54, no. 23-24 (2011): 5077-5086.
[9] Liu, Yang, Yongju Zhang, and Lixing Zhou. "Numerical study on bubble-liquid two-phase turbulent hydrodynamics in extremely narrow shape bioreactor." *International Communications in Heat and Mass Transfer* 108 (2019): 104286.
[10] Wah-Yen, Tey, Yutaka Asako, Nor Azwadi Che Sidik, and Goh Rui-Zher. "Governing equations in computational fluid dynamics: Derivations and a recent review." *Journal of Progress in Energy and Environment* 1 (2017): 1-19.
[11] Gui, Nan, Jie Yan, Zhenlin Li, and Jianren Fan. "Direct numerical simulation of confined swirling jets." *International Journal of Computational Fluid Dynamics* 28, no. 1-2 (2014): 76-88.
[12] Nagata, Takayuki, Taku Nonomura, Shun Takahashi, Yusuke Mizuno, and Kota Fukuda. "Direct numerical simulation of flow around a heated/cooled isolated sphere up to a Reynolds number of 300 under subsonic to supersonic conditions." *International Journal of Heat and Mass Transfer* 120 (2018): 284-299.
[13] Orazzo, Annagrazia, and Sébastien Tanguy. "Direct numerical simulations of droplet condensation." *International Journal of Heat and Mass Transfer* 129 (2019): 432-448.
[14] Chu, Xu, Guang Yang, Sandeep Pandey, and Bernhard Weigand. "Direct numerical simulation of convective heat transfer in porous media." *International Journal of Heat and Mass Transfer* 133 (2019): 11-20.
[15] Nicoud, Franck, and Frédéric Ducros. "Subgrid-scale stress modelling based on the square of the velocity gradient tensor." *Flow, turbulence and Combustion* 62, no. 3 (1999): 183-200.
[16] Inagaki, Masahide, Tsuguo Kondoh, and Yasutaka Nagano. "A mixed-time-scale SGS model with fixed model-parameters for practical LES." *J. Fluids Eng.* 127, no. 1 (2005): 1-13.
[17] Kim, Minwoo, Jiseop Lim, Seungtae Kim, Solkeun Jee, Jaeyoung Park, and Donghun Park. "Large-eddy simulation with parabolized stability equations for turbulent transition using OpenFOAM." *Computers & Fluids* 189 (2019): 108-117.
[18] Choi, Haecheon, and Parviz Moin. "Grid-point requirements for large eddy simulation: Chapman's estimates revisited." *Physics of fluids* 24, no. 1 (2012): 011702.
[19] Badoe, Charles E., Zheng-Tong Xie, and Neil D. Sandham. "Large Eddy simulation of a heaving wing on the Cusp of transition to turbulence." *Computers & Fluids* 184 (2019): 64-77.
[20] Arora, Konark, Kalyana Chakravarthy, and Debasis Chakraborty. "Large eddy simulation of supersonic, compressible, turbulent mixing layers." *Aerospace Science and Technology* 86 (2019): 592-598.
[21] Toubiana, Ephraïm, Rémi Gautier, Daniel Bougeard, and Serge Russeil. "Large Eddy Simulation of transitional flows in an elliptical finned-tube heat exchanger." *International Journal of Thermal Sciences* 144 (2019): 158-172.
[22] Argyropoulos, C. D., and N. C. Markatos. "Recent advances on the numerical modelling of turbulent flows." *Applied Mathematical Modelling* 39, no. 2 (2015): 693-732.
[23] Launder, B. E., D. B. Spalding. "The numerical computation of turbulent flows. "*Computer Methods in Applied Mechanics and Engineering* 3, no. 2 (1974): 269–289.
[24] Yakhot, V., S. A. Orszag, S. Thangam, T. B. Gatski, C. G. Speziale. "Development of turbulence models for shear flows by a double expansion technique. " *Physics of Fluids A* 4, no. 7 (1992): 1510–1520.
[25] Shih, T. H., W. W. Liou, A. Shabbir, Z. Yang, J. Zhu. "A new k-ε{lunate} eddy viscosity model for high reynolds number turbulent flows. " *Computers and Fluids* 24, no. 3 (1995): 227–238.

[26] Wilcox, David C. "Reassessment of the scale-determining equation for advanced turbulence models." *AIAA journal* 26, no. 11 (1988): 1299-1310.
[27] Menter, Florian R. "Two-equation eddy-viscosity turbulence models for engineering applications." *AIAA journal* 32, no. 8 (1994): 1598-1605.
[28] Menter, F. R. "Zonal two-equation κ-ω turbulence model for aerodynamic flows." In *23rd AIAA Fluid Dynamics, Plasmadynamics and Lasers Conference, 1993*. 1993.
[29] Yao, Ji, Weibin Yuan, Jianbin Xie, Haipeng Zhou, Mingjun Peng, and Yong Sun. "Numerical simulation of aerodynamic performance for two dimensional wind turbine airfoils." *Procedia Engineering* 31 (2012): 80-86.
[30] Tey, Wah Yen, Ryan Yuen Wye Hong, Yutaka Asako, Hooi Siang Kang, and Khai Ching Ng. "Analysis on Computational Efficiency of Convection Discretisation Schemes in SIMPLE Algorithm." *Journal of Advanced Research in Fluid Mechanics and Thermal Sciences* 58, no. 1 (2019): 100-117.
[31] Von Doenhoff, Albert E. *Theory of Wing Sections: Including a Summary of Airfoil Data*. Dover Publ, 1959.
[32] Johansen, Jeppe, and Jens N. Sørensen. "Prediction of laminar/turbulent transition in airfoil flows." *Journal of aircraft* 36, no. 4 (1999): 731-734.
[33] Ahmed, Tousif, Md Tanjin Amin, SM Rafiul Islam, and Shabbir Ahmed. "Computational study of flow around a NACA 0012 wing flapped at different flap angles with varying Mach numbers." *Global Journal of Research In Engineering* (2014).
[34] Jehad, D. G., G. A. Hashim, A. K. Zarzoor, and CS Nor Azwadi. "Numerical Study of Turbulent Flow over Backward-Facing Step with Different Turbulence Models." *Journal of Advanced Research Design* 4, no. 1 (2015): 20-27.